scientific reports

Check for updates

OPEN

Behavior of layer jamming plate with tunable stiffness and its near wake structure in cross flow

Xiao Yang[1], Shangke Guo[1] & Hanfeng Wang[1,2]✉

As the demand for sustainable energy increases, ensuring the reliability and durability of the wind energy infrastructure has become increasingly critical. This study introduces an innovative variable stiffness structure called a layer jamming plate (LJP) for wind barriers, inspired by natural organisms and layer jamming mechanisms. The proposed structure is composed of a flexible PET film bag, internal photocopy paper material, and a vacuum-driven system and features adaptability, robustness, wide applicability, and low mechanical failure rates. LJP can actively and dynamically adjust its stiffness and shape, thereby altering flow field structures and structural loads. Building on theoretical modeling, this study evaluates the performance of the LJP through three-point bending tests, wind tunnel experiments, and particle image velocimetry (PIV). The experimental results indicate that the LJP is highly sensitive to the number of layers (*n*) and vacuum pressure (*p*), exhibiting a stiffness range that varies approximately n^2. Furthermore, within a wind speed range of 0–16 m/s, the LJP demonstrates two distinct dynamic behavior modes: static bent and flapping. By adjusting the vacuum pressure, the structure can transition between these modes, effectively managing its motion response and wind resistance and altering its flapping state. In conclusion, LJP offers a sustainable solution for wind barrier systems, improving stability and efficiency. This study paves the way for further research on integrating this technology with other smart materials to enhance wind energy control and flow field optimization.

Keywords Tunable stiffness, Layer jamming plate (LJP), Wind barrier, Near wake, Active control

In contrast with structures with high rigidity in engineering, organisms in nature show significant flexibility when they face surrounding flow, e.g., swinging of fish[1], raising of bird feathers during its landing[2] and reconfiguration and flapping of tree leaves in strong winds[3,4]. Extensive studies have been conducted to investigate the coupling behaviors between flexible structure and fluid flow, and their applications in flow control. Compared to active control strategies[5–7], such flexible systems exhibit stronger adaptability, simpler configuration, and higher reliability. These studies often simplify flexible structures as filaments or flat plates. The former can be considered as a two-dimensional (2D) plate, thus, it is also referred to as a flexible plate hereafter for simplicity. It is worth mentioning that flexible plate may also be named as flexible membrane, film and sheet et al., in references, emphasizing its geometric characteristic, with the thickness which is negligibly smaller than its length and width. Once the incoming velocity (U_∞) exceeds a critical value (U_c), flow-induced vibration of the flexible plate occurs, which is of special interest in energy harvesting from the surrounding flow for self-powered sensor nodes[8–11]. Moreover, the abundant vortices generated by the flapping plate can also be utilized in flow control. For example, both heat transfer and mass mixing can be significantly enhanced via flapping flaps[12–16]. Besides, a flapping plate was successfully used to suppress flow separation from forward and backward steps[17–19], and also the aerodynamic forces and flutter of bluff bodies[20,21].

Previous studies have shown that the effectiveness of flow control using flexible plates is significantly influenced by their specific dynamic responses, such as static deformation or flapping motion. Generally, the configurations of a flexible plate can be classified into three typical categories: standard flags (along the flow, fixed at its leading edge), inverted flags (along the flow, fixed at the trailing edge) and flexible plates normal to the incoming flow[22,23]. Given a certain configuration, the behavior of the flexible plate of a perfectly elastic material is dominated by two principal non-dimensional parameters, K_b and M_s, defined as

[1]School of Civil Engineering, Central South University, Changsha, China. [2]National Engineering Research Center of High-Speed Railway Construction Technology, Changsha, China. ✉email: wanghf@csu.edu.cn

$$K_b = \frac{B}{\rho_f U_\infty^2 L^3}, M_s = \frac{\rho_s h}{\rho_f L} \quad (1)$$

where $B = Eh^3/12(1-v^2)$ is the bending rigidity, E is the elastic modulus, h is the thickness, L is the length, v is the Poisson's ratio, and ρ_s and ρ_f are the densities of the plate and fluid, respectively. Thus, K_b can be considered as the ratio of the plate's bending force and the fluid's inertial force[23]. A high K_b value indicates a plate with high rigidity, and vice versa. Obviously, for a given flexible plate in flow control, its behavior is only determined by U_∞ and the corresponding K_b, since all other parameters are fixed. For a wall-clamped flexible plate normal to the flow, Lee et al.[13] suggested that when $K_b \geq 0.14$, the flexible plate flaps irregularly with very small amplitude at its tip edge; when $0.08 \leq K_b < 0.14$, the plate becomes stationary bended along the wind; when K_b further decreases to less than 0.08, the flexible plate flaps periodically with large amplitude, generating a series of flapping-induced vortices (FIVs) downstream, which have been successfully utilized in flow control[24–26]. That is, the designed optimal control scenario may not be achieved for variable incoming flow conditions[27]. A possible solution is to adjust B of the flexible plate to maintain its K_b, i.e., keeping the flexible plate in flapping status, which is optimal for its application in flow control at various U_∞ values.

Fortunately, tunable stiffness structures based on different techniques have been widely studied in the field of soft robots. Yang et al.[28] proposed a structure mimicking human finger joints via shape memory polymers (SMPs), which are capable of transitioning between rubbery and glassy states at different temperatures. Shintake et al.[29] utilized liquid metal polymer actuators (LMPAs) to achieve reversible stiffness modulation through Joule heating with controllable current. Okatani et al.[30] developed a magnetorheological fluid-based system with tunable stiffness by manipulating magnetic fields.

Disturbance-based tunable stiffness structures offer higher potential stiffness compared to SMPs and LMPAs, and do not depend on electric, magnetic or temperature variations, which may limit the adaptability of SMPs and LMPAs to specific tasks and environments. In the pioneering research, Brown et al.[31] developed a universal soft gripper using granular jamming, enabling tunable stiffness to grasp objects with different shapes and surface properties. Subsequent studies by the same team[32] demonstrated improved gripper speed, fault tolerance, and placement accuracy through the introduction of positive and negative pressure. Apart from serving as a tunable stiffness component in soft grippers, granular jamming has found applications in minimally invasive surgery, wearable haptics, and smart fabrics[33,34].

Despite the advantages of granular jamming, it requires a large volume of granular material to achieve sufficient stiffness when jammed and lacks tensile support[35]. To overcome these constraints, researchers have developed layer jamming, which replaces granules with thin, flexible sheets for a more compact design and increased the bending moment capacity. Early applications of layer jamming include wearable haptic display system[36], providing varied mechanical feedback in human–machine interactions. Bureau et al.[37] proposed variable stiffness modular units to aid limb rehabilitation patients with appropriate orthotic braces. Kim et al.[38] developed a snake-like manipulator that maximizes the stiffness variation between jammed and unjammed states by helically arranging thin layers. Choi et al.[39] introduced a novel sliding linkage-based layer jamming (SLLJ) mechanism, enabling movement in the linear, pitch, and yaw directions by adjusting the stiffness in multiple directions. Ibrahimi et al.[40] proposed a multi-chamber structure that effectively adjusts the device shape and stiffness and demonstrated the ability to tune the stiffness over two orders of magnitude.

In addition to applications, the mechanical properties of layer jamming structures have been studied through both analytical models and numerical simulations. Narang et al.[41] provided one of the initial analysis models based on Euler–Bernoulli beam theory to predict the stiffness of a cantilever 2-layer jamming structure. This work generated finite element models to predict the mechanical response of multi-layer jamming structures under arbitrary loading and boundary conditions[42,43]. Caruso et al.[44] introduced a comprehensive analytical model, which can predict the behavior of layer jamming structures of all deformation phases. This model provides critical theoretical support for the design of variable stiffness applications in soft robotics. More recently, Caro and Carmichael[45] reviewed the mechanisms and applications of tunable stiffness structures using jamming components.

Inspired by the idea of the above mentioned tunable stiffness structure using jamming layers[36,37,42], in this paper, we propose a tunable stiffness layer jamming plate (LJP) and study its flow-structure coupling characteristics in crossflow, which is crucial for the robustness in its application in flow control. The paper is organized as follows: Section "Fabrication of the LJP and its mechanical properties" introduces the fabrication of the tunable stiffness LJP and its mechanical properties. Section "Behavior of the LJP in cross flow and its near wake structure" discusses the behaviors of the LJP in cross flow, including its aerodynamic drag and near wake flow structures of different statuses. Possible applications of the LJP in flow control and active wind barrier[10] are preliminarily discussed in Section "Conclusion and application", and conclusions are outlined in Section "Conclusion and application".

Fabrication of the LJP and its mechanical properties

Fabrication of the LJP

The tunable stiffness structure using jamming components can be largely classified into three categories: granular jamming, fiber jamming and layer jamming[43]. Considering that the present paper focuses on the possible application of tunable stiffness plate in flow control, layer jamming structures are thus utilized[41,44,45]. The general working mechanism of LJP is to transform the inner layers from an unjammed free-slipping state to a jammed friction state, by changing the vacuum pressure inside the envelope. The friction between layers varies with the vacuum pressure, thus achieving tunable stiffness.

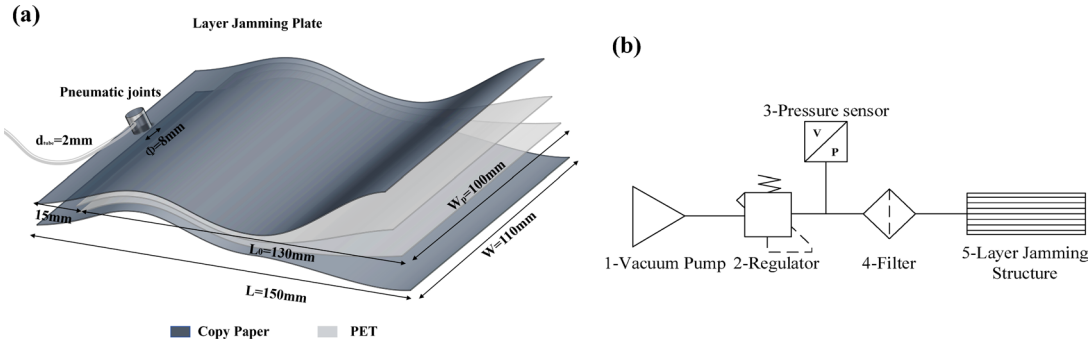

Fig. 1. Sketch map of the LJP: (**a**) the components and dimensions of LJP, and (**b**) pressure regulation system for the LJP.

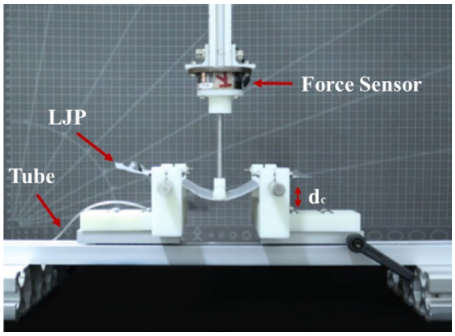

Fig. 2. Experimental setup of bending tests for the LJP.

Name	Model	Parameters
Vacuum Pump	Fujiwara, V1500-50	Vacuum Level: ≥ − 0.098 MPa, Flow Rate: ≤ 203 L/min
Vacuum Pressure Regulator	SOLH, IRV10-C06	Pressure Setting Range: 0 to − 100 kPa
Vacuum Pressure Gauge	SOLH, ZSE30A-01-P-L	Operating Pressure Range: 0 to − 101.0 kPa
Force Sensor	ATI, Mini40	Measurement Range: F_x, $F_y \leq 20$ N, $F_z \leq 60$ N, Accuracy: ± 1%

Table 1. Equipment used for testing the mechanical properties of the LJP.

To fabricate the LJP, several pieces of copy paper (80 g) were placed inside a polyethylene terephthalate (PET) airtight envelope. The thicknesses of the envelope and copy paper were 0.16 mm and 0.1 mm, respectively. The total length (L) and width (W) of the LJP were 150 mm and 110 mm, respectively, as shown in Fig. 1. The sealed edges of the PET envelope were approximately 5 mm in width, minimizing its effects on the overall behavior of the LJP. The open edge of the PET envelope was sealed after the jamming layers (i.e., the copy paper) were placed inside, forming a rectangular airtight envelope. Note that to avoid an additional restrictive effect at the edges of the copy paper during bending, its length was slightly smaller than the envelope. Finally, a polyurethane (PU) tube with a diameter of 2 mm was installed near the edge of the PET envelope via a vacuum pneumatic joints (PA-08), as shown in Fig. 1(a). The PU tube was connected to a vacuum pump, which allowed adjustment of the inner pressure of the PET airtight envelope. The vacuum system was powered by an intelligent oil-free vacuum pump (model V1500-50, Fujiwara), with the vacuum pressure precisely regulated and monitored through a pressure regulator and gauge, as shown in Fig. 1(b).

To validate the theoretical model of the LJP, a series of three-point bending tests were conducted. The LJP was simply supported by two 3D-printed hinge supports to test its deformation at different loads (Fig. 2). The force exerted on the LJP was measured via an ATI Mini40 force balance and recorded by a LabVIEW interface. The equipment used for this test is listed in Table 1. We also measured the mechanical properties of different materials of the LJP, as outlined in Table 2, to facilitate subsequent modeling and calculations. Furthermore, it is worth mentioning that all test in this section were repeated five times to ensure statistical robustness, as recommended by Blanc et al.[46].

Specification	Value
Frictional coefficient μ	0.60
Vacuum level p	0, 20, 40, 60, 80 kPa
No. of layers n	2, 4, 8, 12
Width of flaps W	110 mm
Overlapped length of flaps L	150 mm
E of copy paper, E_{paper}	3 GPa
Thickness of copy paper, h_{paper}	100 µm
E of PET, E_{pet}	3 GPa
Thickness of PET, h_{pet}	160 µm

Table 2. Main parameters related to the mechanical properties of the LJP.

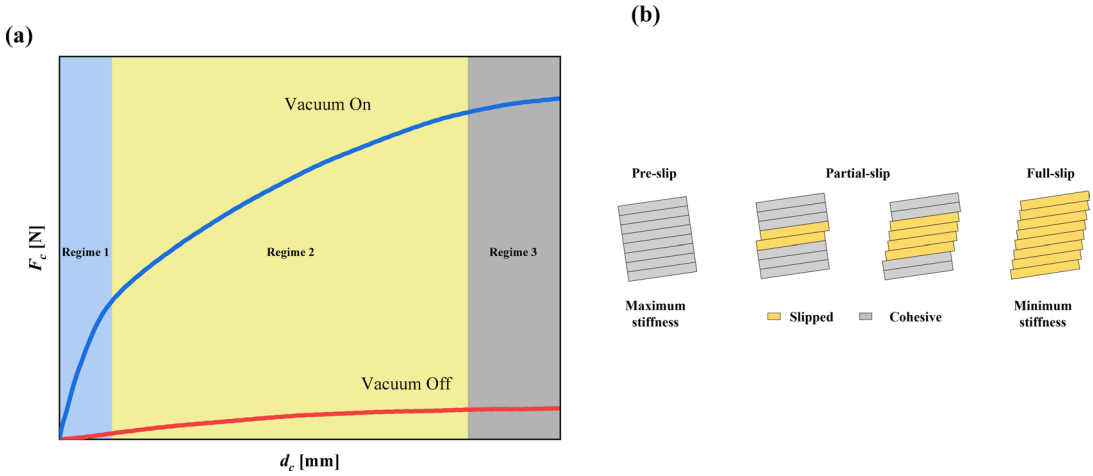

Fig. 3. Load-displacement curves of LJP (**a**) before and after vacuum application and (**b**) corresponding sliding statuses between layers.

Modeling and characteristics of the LJP

The mechanical properties of multi-layer structures are widely used to predict the behavior of laminated composites[41,44,47]. Although complex slip propagation models can accurately predict the behavior of laminated composites. For LJP, friction and vacuum pressure are the primary controlling factors. Therefore, this study utilizes a simplified model to estimate the stiffness range of the LJP, which is verified through three-point bending tests.

For multi-layer tunable stiffness structures, the Euler–Bernoulli assumption is typically used to define their bending stiffness. The stiffness of a simply supported beam is given by the formula: $k = \frac{48EI}{L^3}$, where k is the stiffness, E is the Young's modulus, I is the moment of inertia of the cross-section, and L is the length of the beam. The moment of inertia for a single rectangular cross-section is $I_s = \frac{bh^3}{12}$, where b and h are the width and height, respectively. For an n-layer unjammed structure, if each layer can slide freely between each other, the total moment of inertia is $I_u = nI_s$. When vacuum is applied, inter-layer sliding is prevented, and the structure behaves as a single entity, with the moment of inertia given by: $I_j = b(nh)^3/12 = n^2 I_u$. It can increase the stiffness of the element in n^2 order as n increases. Structures utilizing layer jamming demonstrate the ability to vary stiffness within the range of the two extreme states mentioned above. This versatility enables easy adjustment by leveraging changes in the structure's vacuum level, thereby meeting the requirements of different environmental conditions.

In addition to the theoretical model of slip propagation in LJP, we can further understand its bending stiffness characteristics by examining the load-displacement curve, as shown in Fig. 3. For the unjammed state, i.e., when the vacuum is off, the load-displacement curve is expected to be approximately linear, as shown in Fig. 3(a), because all the layers bend independently of each other. For the jammed state, i.e., the vacuum if on, the load-displacement curve can be divided into three typical regimes, as illustrated in Fig. 3(b). In regime 1 (None-slip regime), because the shear stress between layers remains below the friction limit, the LJP behaves like a single beam with the maximum stiffness. In regime 2 (Partial-slip regime), the LJP enters a partial-slip state with increasing load, where slip starts from the central interface and propagates outward. The load-displacement curve becomes nonlinear with decreasing stiffness. In regime 3 (Full-slip regime), the load increases linearly and slowly with increasing deflection, which is qualitatively similar to that observed in the unjammed case. Notably, although slip occurs between all the layers in the full-slip regime, the corresponding stiffness is much higher

than that of the unjammed case, especially for LJP with more layers, because of the additional friction between layers when the vacuum is on.

Figure 4 presents the load-displacement curves for the tested LJPs with $n = 2$, 4, 8, and 12, respectively. The results with the vacuum level p ranging from 0 to 80 kPa are compared with the theoretical range as discussed above (for the sake of brevity in the subsequent text, we omit the symbol for vacuum pressure, while the intended meaning remains unchanged). To quantify the bending stiffness in the three-point bending test, it is defined as the ratio of the applied force to the deflection of the LJP, i.e., $k = F_c/d_c$, where F_c and d_c represent the mean vertical force and displacement, at the mid-span of the LJP respectively. The shadow area under each line indicates the maximum range of F_c among the five repeated tests for each case.

As expected, for all the tested LJPs with different numbers of layers, the bending stiffness increases significantly with the vacuum level p. Particularly, the overall behavior of the load-displacement curves changes from linear to nonlinear with increasing p, as shown in Fig. 4. At $p = 0$ kPa, the LJP exhibited an obvious linear response, especially at relatively small displacements. The stiffness of the LJPs increases significantly with increasing p and n. Moreover, the maximum stiffness is very close to the upper boundary derived using the non-slip assumption, especially for the LJPs with more layers at a smaller F_c and higher p, as shown in Fig. 4. Notably, the linear range of the load-displacement curves also increases with n and p, suggesting the expansion of the applicable range of the none-slip assumption (as shown in Fig. 3). The secant slope k at $d_c = 30$ mm was defined as the mean stiffness, which was then used to quantify the effects of both n and p on the stiffness of the LJPs, as shown in Fig. 5. For example, the mean stiffness of the LJP with $n = 12$ at $p = 80$ kPa is 32 times greater than that at $p = 0$ kPa. Obviously, the enhancement in the mean increase $\bar{k}$ with increasing p is more remarkable when p is relatively small, which becomes less obvious at higher p. This may be ascribed to the nonlinear increase in the friction between layers with increasing normal force.

To validate the controllability of the LJP during deformation, an additional load-displacement test was conducted for the LJP with $n = 12$, as shown in Fig. 6. Initially, when the vacuum is off, the stiffness of the LJP is very low, as shown by the first section of the solid line, although the load-displacement curve remains linear. Once the center displacement reached 14 mm, a vacuum pressure with $p = 80$ kPa was applied to the LJP, as indicated by the red dot. Obviously, a significant increase in stiffness was achieved, regardless of the pronounced nonlinear behavior in the load-displacement curve with further increasing F_c, which is similar to that observed when the vacuum was initially applied, as shown by the upper dashed line. This observation indicates that LJP exhibits strong adaptability and repeatability under varying vacuum pressures.

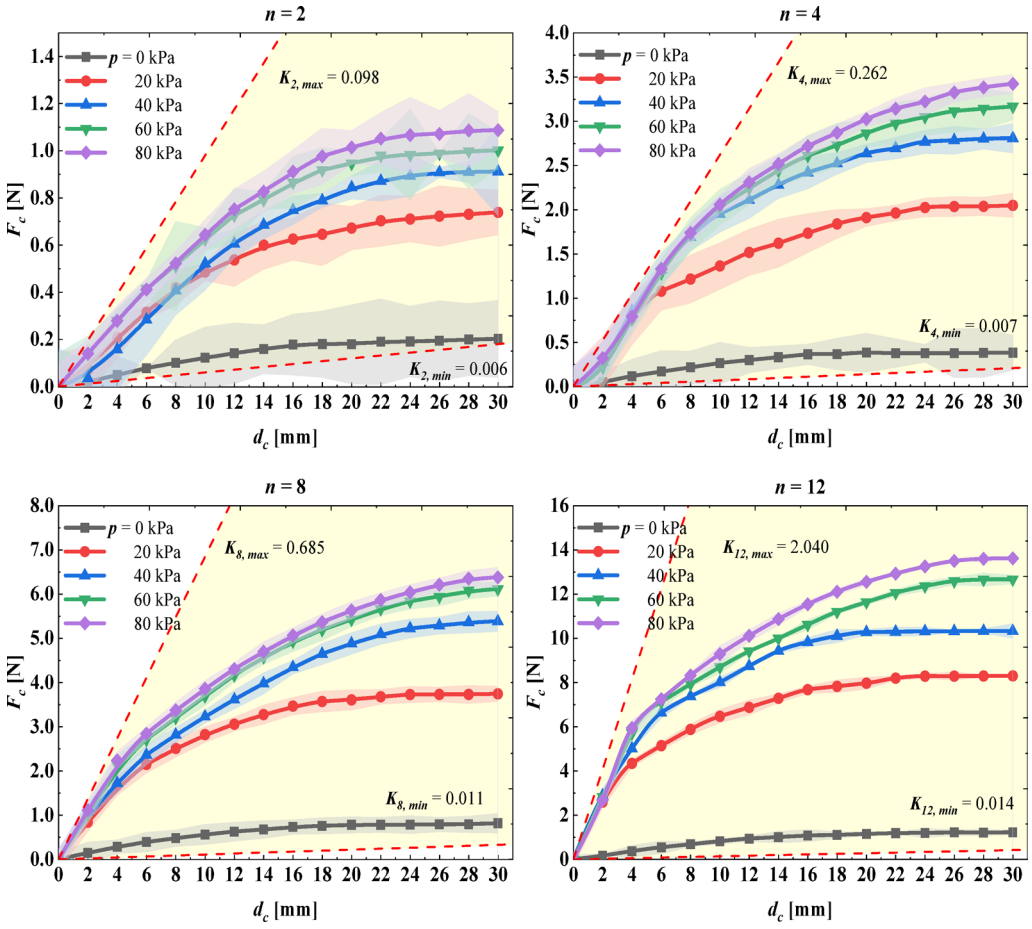

Fig. 4. Load-displacement curves of the LJPs with different numbers of layers.

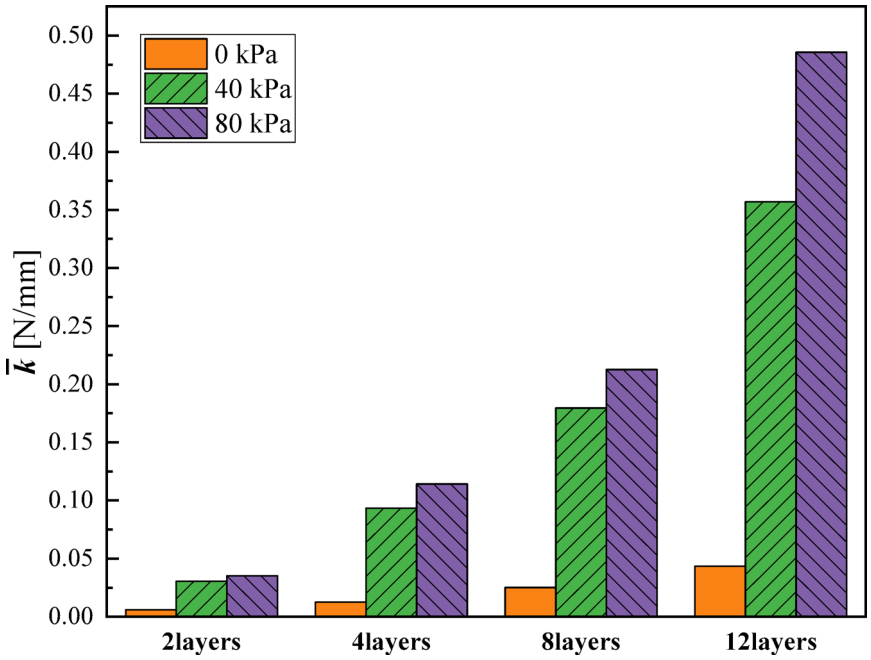

Fig. 5. Dependence of the mean stiffness $\overline{k}$ on the vacuum level p for LJPs with different layers.

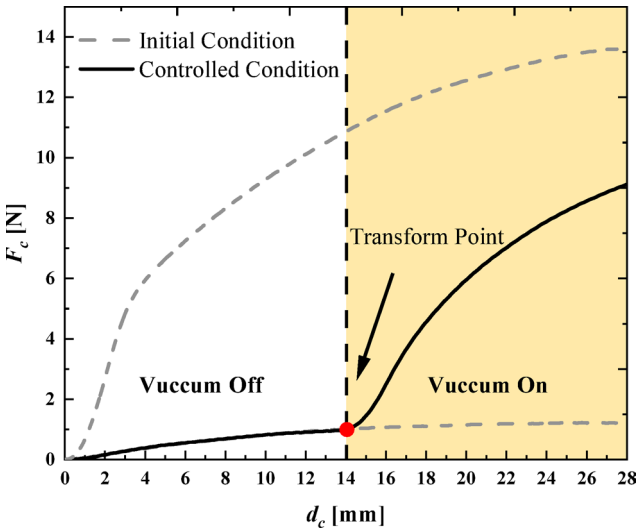

Fig. 6. Load-displacement curve of the LJP with the vacuum pressure applied during its deformation.

These preliminary findings confirm the substantial tunability of the stiffness of LJP under vacuum conditions, providing essential foundational data for subsequent investigations. The capacity to modulate stiffness based on the number of layers and vacuum pressure offers a robust framework for exploring the performance of LJP in more complex environments.

Behavior of the LJP in cross flow and its near wake structure

Experimental setup and incoming flow conditions

The experiments were conducted in an open-loop low-speed wind tunnel featuring a test section measuring 0.45×0.45 m^2 and extending 1.2 m in length. The test section was constructed with acrylic plates to allow for optical access. Operating within a velocity range of 0.1–40 m/s, the wind tunnel maintained a turbulence intensity of 0.5% in the test section. The incoming flow velocity (U_∞) ranged from 0 to 16.0 m/s for the present test. A bracket was installed at the upper surface of the test section, as shown in Fig. 7, which was equipped with an inside tube line to connect the tested LJP and vacuum pump. The tested LJP, with $L_0 = 130$ mm and $W_0 = 110$ mm, was vertically clamped at its top edge via the bracket.

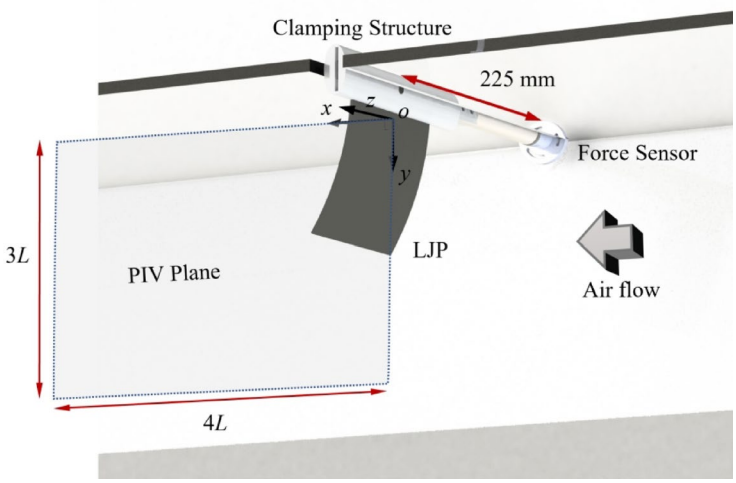

Fig. 7. Experimental setup in the wind tunnel.

Measurement techniques

The flow field downstream of the LJP was visualized both qualitatively and quantitatively via 2D particle image velocimetry (PIV) and smoke-wire (Hanghua SW-02) techniques, respectively. The aerodynamic drag on the LJP was also measured with a force balance (ATI mini-40). The PIV measurement was conducted at the central lateral plane in the wake of the LJP, as shown in Fig. 7. The PIV system employed a Hisense Zyla CMOS camera with a resolution of 2560×2160 pixels^2. which was synchronized with a dual pulsing laser at a sampling frequency of 5 Hz. The spatial resolution of the PIV measurement was 90.9 μm/pixel, and the interrogation window was 32×32 pixel^2, with a 50% overlap in both directions.

The tracing particles used for PIV measurement were atomized paraffin provided by a liquid droplet seeding generator (Flow Tracker 700CE). The diameter of the tracing particles was approximately 1–3 μm. A total of 1000 instantaneous flow fields were captured for the cases with and without vacuum applied to the LJP, referred to as "Vacuum on" and "Vacuum off", respectively. Smoke-wire flow visualization was also conducted in the central lateral plane, identical to the PIV measurement. An ATI mini-40 force sensor was used to measure the drag of the LJP, with a sampling frequency of 1000 Hz and a sampling duration of 60 s.

The behavior of the LJP was recorded via a high-speed camera at a shooting frame of 960 fps. Both the flapping configuration and frequency of the LJP could be obtained by analyzing the recorded video.

Behavior of the LJPs in cross flow

The behavior of the LJP with $n = 2$ in typical cases is shown in Fig. 8. When $U_\infty = 3.6$ m/s, which is lower than the critical wind speed U_c of the LJP with $p = 0$ kPa, the LJP bends under the incoming flow. This deformation of the LJP generates an elastic restoring force that tends to bring it back to its equilibrium position. Eventually, a balance is established between this elastic force and the hydrodynamic force acting on the LJP surface, and the LJP settles into a static bent mode (Fig. 8a). When the vacuum level p increases to 40 kPa (Fig. 8b), the curvature of the LJP reduces noticeably, because of the increase of its bending rigidity as discussed in Section "Fabrication of the LJP and its mechanical properties".

When U_∞ increases to 11.2 m/s, the behavior of the LJP becomes completely different for $p = 0$ and 40 kPa, as shown in Fig. 8c and d. When the vacuum level $p = 0$ kPa, the LJP flaps with large amplitude (Fig. 8c), similar with that observed by Liu et al.[18] for a thin flexible film in cross flow. Complex change in the LJP configuration occurs during its flapping cycle. Particularly, the motion of LJP is not always in phase along its length L. This observation is to some extent similar with the travelling wave occurs in the flapping film in separated shear flow, as reported by Liu et al.[19] and Wang et al.[27]. The flapping LJP may effectively disperse the incoming flow, reducing the impact of wind loads on downstream structures[10], which will be explored in detail in future work. The periodic flapping of the LJP suggests that $U_\infty = 11.2$ m/s exceeds the U_c for the LJP with $p = 0$ kPa. In the flapping mode (Fig. 8c), the hydrodynamic force exerted on the LJP fluctuates periodically with the generation and shedding of vortices. This force alternates with the elastic restoring force in dominating the LJP's flapping, thereby inducing alternating upstroke and downstroke flapping motions. Hence, this flow-induced flapping mechanism also falls into the category of vortex-induced vibration[48]. However, once vacuum is on with $p = 40$ kPa (Fig. 8d), the flapping behavior ceases completely, replaced by static bending in flow direction. That is, it is possible to manipulate the vacuum level p of the LJP to modify its stiffness, thus effectively control the behavior, i.e., static bending or flapping, of the LJP in cross flow.

The behavior of a flexible plate in cross is dominated by its dimensionless rigidity K_b, as defined in Eq. (1), where the numerator and denominator can be considered as the bending force of the plate and the fluid inertial force[23], respectively. Obviously, for a certain LJP, its B can be changed by adjusting its vacuum level p, thus effectively regulating its behavior by manipulating K_b. On the basis of our experiments, the tunable range of K_b for the present tested LJPs with different layer number n are show in Fig. 9, accompanied with the 'flapping zone' where flapping of the LJPs occurs. For a certain LJP shown in Fig. 9, the lower and upper boundary of K_b

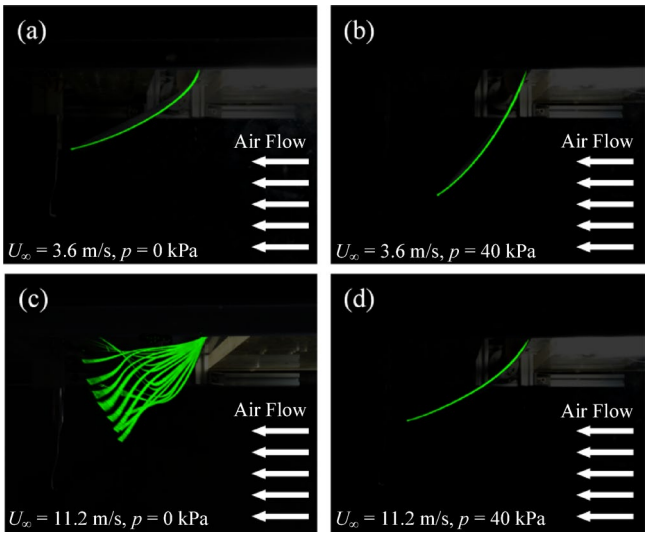

Fig. 8. Image of the LJP with $n = 2$ at typical U_∞ and p.

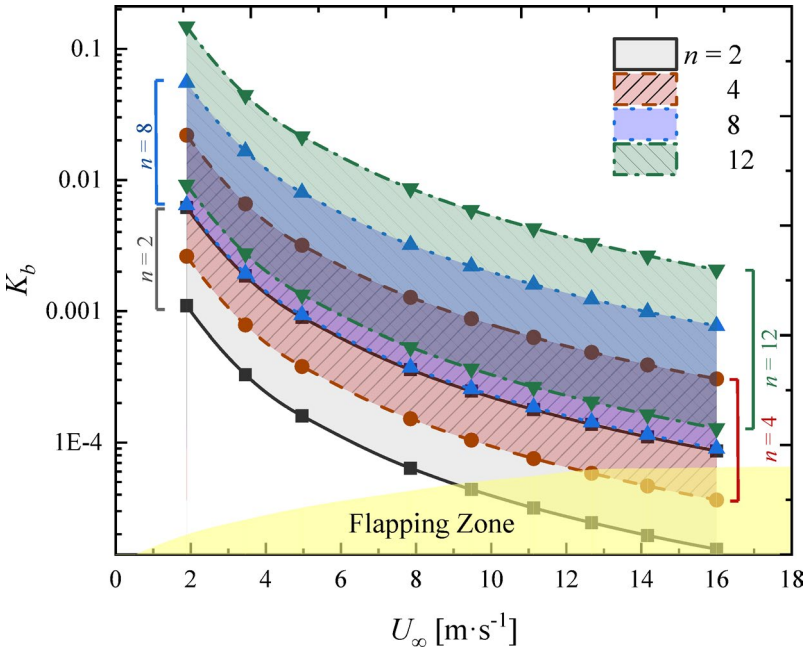

Fig. 9. Adjustable range of the dimensionless rigidity K_b of the LJPs.

correspond to the lowest and highest vacuum level p, i.e. $p = 0$ and 80 kPa, respectively. For the LJPs with $n = 2$ and 4, the adjustable K_b range partially overlaps the flapping zone with increasing U_∞, this observation suggests that the behavior, i.e. flapping and statically bending, of these two LJPs can be successfully switched by adjusting its vacuum level p. However, with n increasing to 8 and 12, the adjustable K_b range is always higher than the flapping zone in the presented U_∞ range. This is expected, because K_b increases significantly with increasing n.

Flapping frequency of LJP

Figure 10 illustrates the flapping frequency (f_p) characteristics of the LJP ($n = 2$ and $n = 4$). As U_∞ increases, the flapping frequency of LJP linearly increases. This is attributed to the increased aerodynamic forces acting on the LJP under high-speed flow conditions, leading to a corresponding increase in flapping frequency. Similar observations have been reported in previous studies, such as those involving flexible plates attached to the free end of finite square cylinders and resembling step geometries[18,27]. The presence of this linear relationship suggests that the LJP flapping behavior is largely controlled by flow conditions, thereby having significant implications for the design and engineering applications of LJP and similar membrane structures.

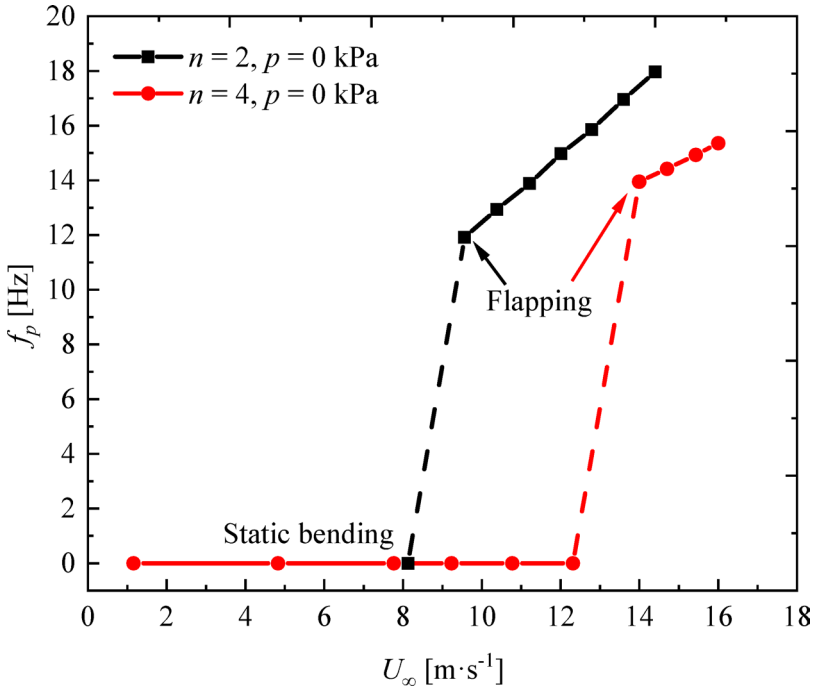

Fig. 10. Flapping frequency (f_p) of the LJP.

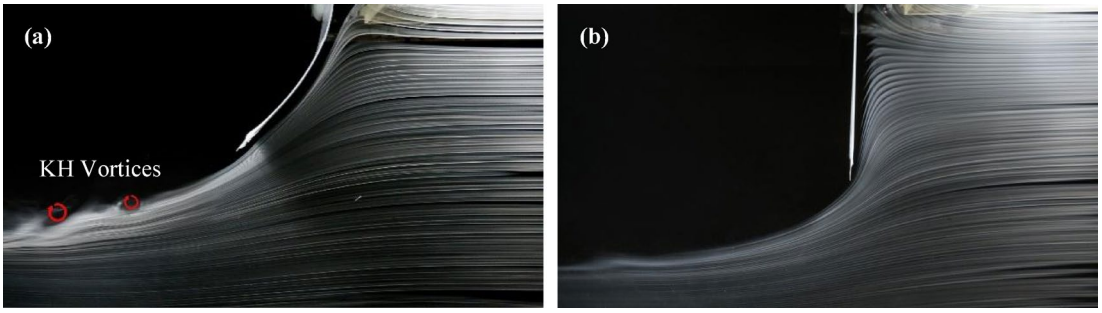

Fig. 11. Smoke-wire flow visualization results of the LJP.

Further analysis revealed that the increase in the flapping frequency is closely related to the material properties of the membrane. Studies indicate that membranes with different material properties may exhibit different flapping behaviors under the same flow conditions. For example, membranes of the same thickness may have different flapping frequencies because of differences in material stiffness. Therefore, in engineering practice, the influence of material selection on the dynamic response of membrane structures needs to be considered to ensure that the designed structures can operate stably under anticipated flow conditions.

Additionally, the flapping frequency of the membrane is also influenced by other factors, such as the pretension of the membrane and external excitations. In practical applications, these factors may cause deviations and variations in flapping frequency, necessitating further experimental research to comprehensively understand these influencing factors and provide more accurate guidance for engineering design.

Flow around the LJPs

The smoke-wire visualization technique is used to analyze the flow field at the rear of the wind barrier, and the results are shown in Fig. 11. A fine high-resistance wire coated in oil stretches across the flow field. The diameter of the wire is 0.2 mm, and its interference with the flow is assumed to be negligible. The wire can produce short bursts of smoke controlled electrically by resistive heating. The smoke follows the air currents, which allows the observer to visualize the flow.

Figure 11 presents the smoke-wire flow visualization results of the LJP. Specifically, the figure shows the following: (a) Smoke-wire photograph of the $n = 12$ LJP at $p = 0$ kPa and $U_\infty = 3.94$ m/s in the static bent mode. (b) Smoke-wire photograph of the $n = 12$ LJP at $p = 80$ kPa and $U_\infty = 3.94$ m/s in a plate-like state. Owing to the high wind speeds during flapping states, these will be further illustrated in the subsequent PIV section. It shows that under vacuum pressure conditions, the LJP can maintain a nearly flat state under relatively low wind speeds.

The incoming wind, blocked by the LJP, flows around it and generates a substantial negative pressure zone. After pressure release, the LJP subsequently bends to enter the static bent mode, reducing resistance and allowing more airflow to pass through. Additionally, numerous Kelvin–Helmholtz (KH) vortices were observed at the trailing edge of the LJP, which is due to the gradient changes in flow velocity and pressure on the surface of the LJP, inducing unstable vortex formations. Particularly at higher wind speeds, shear forces in the flow behind the LJP lead to the formation of KH vortices. The occurrence of these vortices indicates significant fluid separation and reattachment processes in the flow, and their frequency is closely related to factors such as the stiffness, shape, and wind speed of the LJP. This phenomenon is crucial for understanding the flow characteristics around LJP and its implications for wind field optimization.

By connecting multiple units in parallel to form a layer jamming wind barrier, the external vacuum pressure can be adjusted to alter the shape and mechanical properties of the LJP unit. For instance, when the vacuum pressure is high, most of the airflow cannot pass through the wind barrier, creating a larger protective area downstream. Conversely, when the vacuum pressure is low, more airflow can pass through the free space beneath the layer jamming wind barrier, thereby improving the barrier's own load. This has been demonstrated as an effective method for altering the flow field and controlling fluid dynamics.

Figure 12 presents the contours of $\overline{U}$, ω and streamlines in the LJP central plane under different vacuum conditions. The overbar denotes the time-averaged value, which is calculated via the 2000 randomly sampled PIV snapshots. It is noteworthy that for experimental convenience in terms of laser placement and to avoid structural shadowing, the structure was deliberately rotated and placed upside down at the bottom of the test section. Consequently, the gravitational force on the structure exacerbated the bending of the LJP, resulting in slightly different morphological and mechanical characteristics than those discussed earlier. However, it still reflects the efficient and variable nature of the LJP, holding significant reference and research significance.

Figure 12(a) shows the PIV results of the LJP at $p = 0$ kPa and 80 kPa at $U_\infty = 2.2$ m/s. It can be observed that under $p = 0$ kPa, the adaptive bending of LJP results in a smaller negative pressure zone, with a height of approximately $0.6L$ at $x = 2L$ downstream. Conversely, at $p = 80$ kPa, the LJP maintains its shape better, forming a larger recirculation zone. The negative pressure zone at $x = 2L$ downstream reaches a height of approximately $1.8L$. In both scenarios, the normalized wind speed $\overline{U}$ accelerates above the recirculation zone, leading to a large area with $\overline{U} / U_\infty > 1$. Below the recirculation zone, the average flow velocity reverses, with the maximum reverse flow velocity reaching − 0.2. Notably, the acceleration zone is also larger at $p = 80$ kPa. Figure 12(b) shows the PIV results of the LJP at $p = 0$ kPa and 80 kPa at $U_\infty = 15.4$ m/s. Under higher wind speed conditions, at $p = 0$ kPa, the LJP undergoes periodic flapping, generating alternating vortices. These vortices eliminate the recirculation zone, resulting in a more uniform flow field behind the LJP than under the $p = 80$ kPa condition.

To further understand the impact of flapping on the recirculation zone and flow uniformity, Fig. 12(c) presents two instantaneous PIV snapshots captured during the flapping motion. The evolution of vortex structures during the flapping process is further elucidated as follows: when the trailing edge of the LJP deflects upward, a clockwise vortex N1 is generated at the tail. This vortex is convected downstream due to the combined effects of the flapping motion and the induced airflow, promoting the downward movement of the separated shear layer toward the wall and thereby enhancing momentum exchange near the surface. Conversely, when the trailing edge deflects downward, a counterclockwise vortex is formed. Together with N1, it induces a downward flow of fluid toward the wall. These findings show good agreement with the phase-averaged PIV results of flapping flexible membranes reported by Liu et al.[18], with only minor deviations.

These findings align well with the PIV results presented in this study, demonstrating the feasibility of controlling the rigidity and flexibility of LJP through vacuum pressure. This significant adaptability under different wind speed and pressure conditions provides robust support for the stability and effectiveness of LJP in practical applications.

Aerodynamic drag of the LJPs

Figure 13 shows the variations in resistance (RMS) experienced by the LJPs of different layers under various vacuum conditions and incoming flow velocities. It is evident that prior to the onset of flapping, there is a positive correlation between the resistance encountered by the LJP and its layer count, which reflects its stiffness. Greater stiffness results in reduced deformation and increased resistance.

Under vacuum conditions of 0 kPa, LJP with fewer layers experienced lower critical velocities for flapping (U_c). For instance, the LJP with $n = 2$ experiences flapping at 9.4 m/s, whereas the LJP with $n = 4$ exhibits flapping at 12.8 m/s. Notably, the $n = 8$ and 12 configurations do not undergo flapping within the 0–16 m/s range, indicating a higher threshold for flapping onset. Furthermore, the substantial increase in overall resistance is attributed to the significant additional resistance generated by the flapping, particularly due to the relatively large mass of the LJP compared with the experimental model.

Under $p = 40$ kPa, the introduction of negative pressure prevents LJP from experiencing flapping within the tested range of wind speeds. The maximum wind resistance increases with the number of layers in the LJP. For example, the LJP with $n = 12$ results in a wind resistance of up to 2.5 N at 16 m/s, whereas the LJP with $n = 2$ only reaches 0.65 N at the same velocity. Notably, a pronounced nonlinear relationship exists between the wind resistance and wind speed, indicating a transitional state within the LJP. Internal slipping within the structure leads to a reduction in the rate of increase in the wind resistance, which gradually stabilizes. For example, the wind resistance of the LJP with $n = 4$ stabilizes at approximately 0.75 N after 5 m/s.

For LJPs with the same number of layers, the introduction of negative pressure enhances their wind resistance to a certain extent. This effect is more pronounced in LJPs with a greater number of layers. For example, under a wind speed of 5 m/s, the wind resistance under 80 kPa vacuum conditions for the LJP with $n = 4$ is approximately 0.75 N, whereas under 0 kPa conditions, it is approximately 0.25 N, representing a twofold

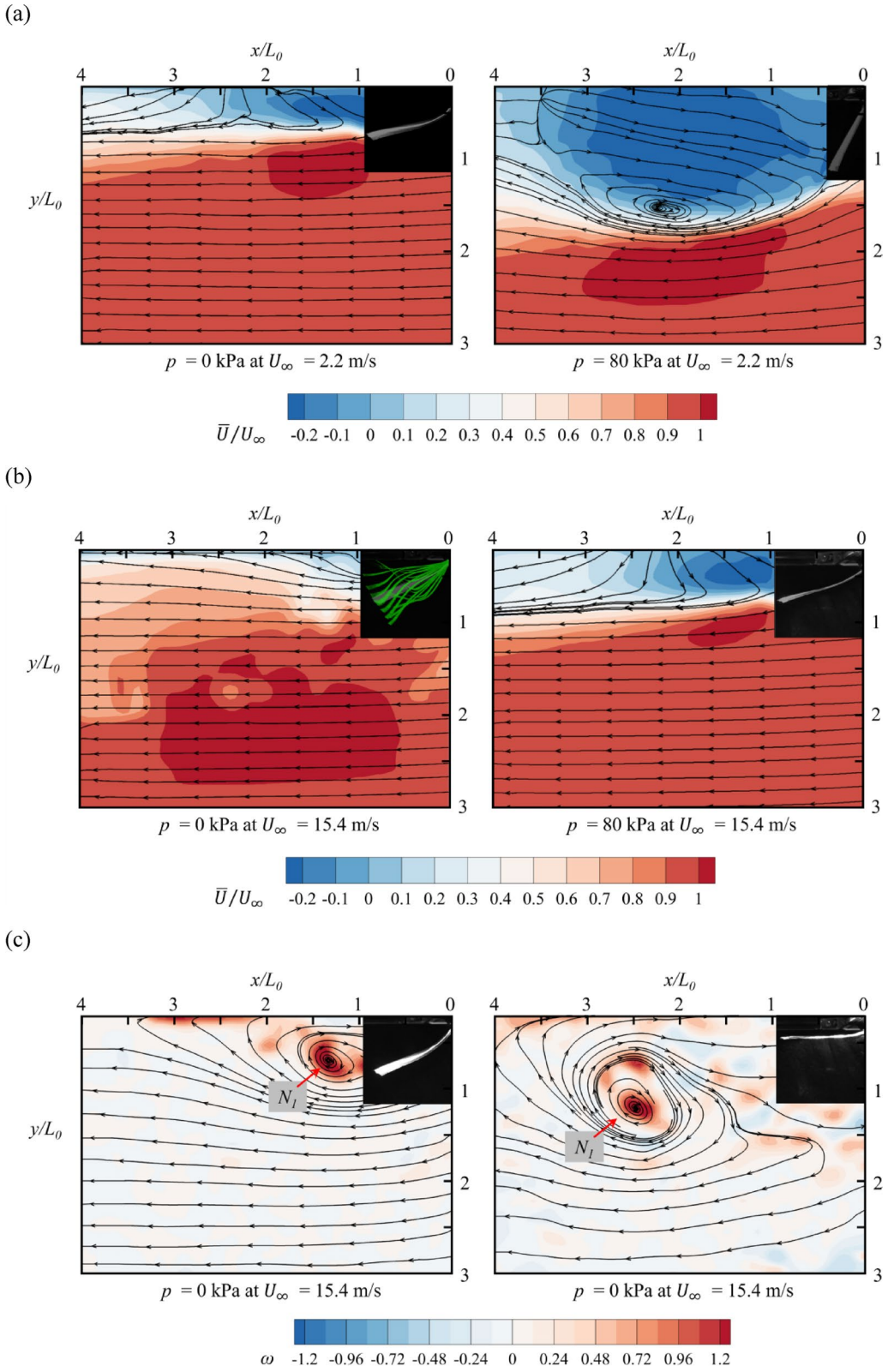

Fig. 12. Contours of U^*, ω and streamlines in the central plane of the LJP ($n=2$): (**a**) $U_\infty = 2.2$ m/s with $p = 0$ kPa and 80 kPa (**b**) $U_\infty = 15.4$ m/s with $p = 0$ kPa and 80 kPa (**c**) Instantaneous vorticity (ω) results during the flapping motion at $U_\infty = 15.4$ m/s with $p = 0$ kPa.

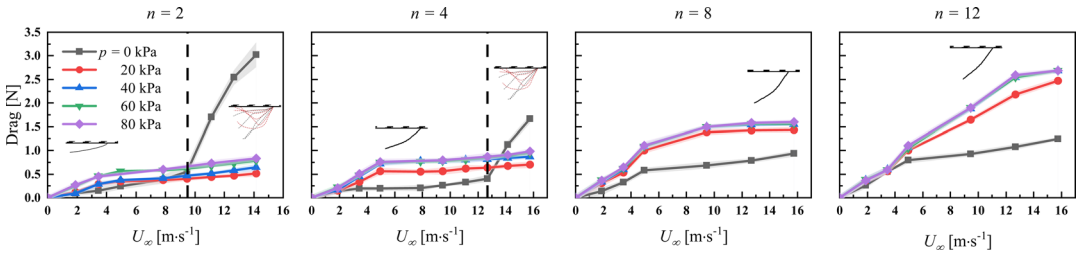

Fig. 13. Drag of LJPs under various wind speeds.

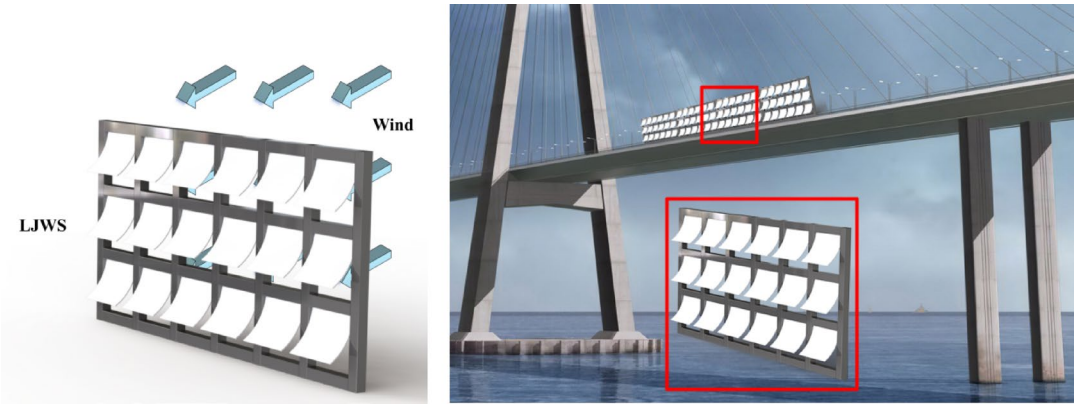

Fig. 14. Schematic diagram of the active wind barrier based on LJP units.

increase. Furthermore, for the LJP with $n=2$ and 4 tested, the introduction of negative pressure significantly increases the critical velocities for flapping and can even suppress flapping occurrence. This undoubtedly provides promising applications for flapping control in future engineering endeavors.

Conclusion and application

This study presents a novel variable stiffness wind barrier design using layer jamming plate (LJP) technology. Through experiments, including three-point bending tests, wind tunnel testing, and particle image velocimetry (PIV), we demonstrated the ability of LJP to adjust stiffness and respond dynamically to wind loads.

The key findings include the following: the LJP stiffness can be adjusted on the basis of the square of the layer count n, confirming the effectiveness of layer variation for stiffness control in wind barrier design. LJP exhibits nonlinear behavior under increasing loads, transitioning through pre-slip, partial-slip, and full-slip stages, highlighting its adaptability. The vacuum pressure can modulate the LJP stiffness, effectively controlling the flapping behavior in wind barrier applications, as shown in the experiments with $n=2$ and $n=4$. The flapping frequency of the structure increases linearly with the wind speed and can be adjusted by changing the vacuum pressure, offering a dynamic control strategy for wind barriers.

This work confirms the potential of LJP technology in wind barrier systems and provides a new approach for wind energy control and flow field optimization, as shown in Fig. 14. The adjustable stiffness and dynamic response capabilities of the LJP provide valuable tools for optimizing wind barrier design. Future research should explore LJP performance under various environmental conditions and its integration with other smart technologies for more sustainable wind energy use.

This work confirms the potential of LJP technology in wind barrier systems and provides a new approach for wind energy control and flow field optimization. As shown in Fig. 14, a combined LJP wind barrier composed of numerous independent LJP units is presented. This new type of wind barrier can address the issues inherent in traditional fixed wind barriers, whose stiffness cannot be adjusted, and those of mechanical adjustable wind barriers, which require high maintenance costs. By regulating interlayer friction via negative pressure, LJP technology enables dynamic stiffness adjustment and optimized ventilation rates, allowing the wind barrier to actively adapt to different wind speed conditions. This significantly enhances the adaptability and robustness of the wind barrier, thereby improving train operational safety. Furthermore, the combined LJP wind barrier allows precise local adjustment of mechanical properties through independent control of individual unit stiffness. When integrated with an adaptive adjustment strategy, it can automatically and dynamically respond to changes in the wind field, further enhancing the overall performance of the barrier. The current research is primarily based on short-term wind tunnel experiments, and there is a lack of durability assessment under long-term wind loads. Future work should include long-term fatigue testing and verify the effectiveness and reliability of the system

under real-world conditions. Future research should also explore LJP performance under various environmental conditions and its integration with other smart technologies for more sustainable wind energy use.

Data availability

All data that support the findings of this study are available from the corresponding author.

Received: 12 December 2024; Accepted: 29 September 2025
Published online: 05 November 2025

References

1. Harvey, S. T., Muhawenimana, V., Müller, S., Wilson, C. A. M. E. & Denissenko, P. An inertial mechanism behind dynamic station holding by fish swinging in a vortex street. *Sci. Rep.* **12**(1), 12660. https://doi.org/10.1038/s41598-022-16181-8 (2022).
2. Brücker, C. & Weidner, C. Influence of self-adaptive hairy flaps on the stall delay of an airfoil in ramp-up motion. *J. Fluids Struct.* **47**, 31–40. https://doi.org/10.1016/j.jfluidstructs.2014.02.014 (2014).
3. Vogel, S. Drag and reconfiguration of broad leaves in high winds. *J. Exp. Bot.* **40**(8), 941–948. https://doi.org/10.1093/jxb/40.8.941 (1989).
4. Zhu, Y. & Shao, C. The steady and vibrating statuses of tulip tree leaves in wind. *Theor. Appl. Mech. Lett.* **7**(1), 30–34. https://doi.org/10.1016/j.taml.2016.12.002 (2017).
5. Zhao, L. et al. Flutter performance simulation on streamlined bridge deck with active aerodynamic flaps. *Comput.-Aided Civ. Infrastruct. Eng.* **39**(12), 1830–1850. https://doi.org/10.1111/mice.13170 (2024).
6. Li, S. et al. Flow control of a surface-mounted finite-length square cylinder using synthetic jets. *Acta. Mech. Sin.* **41**, 325254. https://doi.org/10.1007/s10409-025-25254-x (2025).
7. Li, S. et al. Control of vortex-induced vibrations inrectangular plates: The effects of suction position. *Phys. Fluids* **37**(9), 097121. https://doi.org/10.1063/5.0281907 (2025).
8. Goushcha, O., Elvin, N. & Andreopoulos, Y. Interactions of vortices with a flexible beam with applications in fluidic energy harvesting. *Appl. Phy Lett.* https://doi.org/10.1063/1.4861927 (2014).
9. Fu, X., Bu, T., Li, C., Liu, G. & Zhang, C. Overview of micro/nano-wind energy harvesters and sensors. *Nanoscale* **12**(47), 23929–23944. https://doi.org/10.1039/D0NR06373H (2020).
10. Wang, Y. et al. Multi-functional wind barrier based on triboelectric nanogenerator for power generation, self-powered wind speed sensing and highly efficient windshield. *Nano Energy* **73**, 104736. https://doi.org/10.1016/j.nanoen.2020.104736 (2020).
11. Wu, H. et al. A highly efficient multifunctional wind barrier based on PVDF for power generation in the Qinghai-Tibet railway. *Energ. Technol.* **10**(3), 2100760. https://doi.org/10.1002/ente.202100760 (2022).
12. Ali, S., Menanteau, S., Habchi, C., Lemenand, T. & Harion, J.-L. Heat transfer and mixing enhancement by using multiple freely oscillating flexible vortex generators. *Appl. Therm. Eng.* **105**, 276–289. https://doi.org/10.1016/j.applthermaleng.2016.04.130 (2016).
13. Lee, J. B., Park, S. G., Kim, B., Ryu, J. & Sung, H. J. Heat transfer enhancement by flexible flags clamped vertically in a Poiseuille channel flow. *Int. J. Heat Mass Transf.* **107**, 391–402. https://doi.org/10.1016/j.ijheatmasstransfer.2016.11.057 (2017).
14. Xu, M., Wu, M. & Mi, J. A new type of self-excited flapping jets due to a flexible film at the nozzle exit. *Exp. Therm. Fluid Sci.* **106**, 226–233. https://doi.org/10.1016/j.expthermflusci.2019.04.031 (2019).
15. Zhao, B. et al. Experimental study on heat transfer enhancement by using textile flap oscillation. *Heat Transf. Eng.* **43**(6), 503–515. https://doi.org/10.1080/01457632.2021.1887638 (2022).
16. Qi, X., Qu, X. & Lv, J. Study on the heat transfer enhancement characteristics by flow-induced vibration of inserting polyethylene membrane inside the channel. *Int. J. Therm. Sci.* **196**, 108753. https://doi.org/10.1016/j.ijthermalsci.2023.108753 (2024).
17. Ma, X. & Schröder, A. Analysis of flapping motion of reattaching shear layer behind a two-dimensional backward-facing step. *Phy. Fluids* https://doi.org/10.1063/1.4996622 (2017).
18. Liu, Z., Wang, H. & Zhao, C. Flow over a forward-facing step with a flexible membrane at its leading edge. *Exp. Therm. Fluid Sci.* **146**, 110922. https://doi.org/10.1016/j.expthermflusci.2023.110922 (2023).
19. Liu, Z., Wang, H., Li, J., Li, H. & Zhao, C. Flapping dynamics of a flexible membrane attached to the leading edge of a forward-facing step. *Phys. Fluids* **36**(5), 054114. https://doi.org/10.1063/5.0211188 (2024).
20. Zhao, C., Wang, H., Liu, Z., Alam, M. M. & Tang, H. Near-wake structures of a finite square cylinder with a flapping film at its free end. *Phys. Fluids* **35**(9), 095102. https://doi.org/10.1063/5.0153537 (2023).
21. Zhang, Z., Yin, Y. & Wang, H. Control of the nonlinear flutter of a rectangular cylinder using auxiliary flexible films. *Nonlinear Dyn.* **112**(18), 15741–15756. https://doi.org/10.1007/s11071-024-09834-y (2024).
22. Alben, S., Shelley, M. & Zhang, J. Drag reduction through self-similar bending of a flexible body. *Nature* **420**(6915), 479–481. https://doi.org/10.1038/nature01232 (2002).
23. Yu, Y., Liu, Y. & Amandolese, X. A Review on Fluid-Induced Flag Vibrations. *Appl. Mech. Rev.* https://doi.org/10.1115/1.4042446 (2019).
24. Tan, J., Wang, Z. & Gursul, I. Post-stall flow control on aerofoils by leading-edge flags. *J. Fluid Mech.* https://doi.org/10.1017/jfm.2023.678 (2023).
25. Yin, Y., Wang, H. & Li, H. Effects of flexible films on the aerodynamics of a 5:1 rectangular cylinder. *Exp. Therm. Fluid Sci.* **144**, 110870. https://doi.org/10.1016/j.expthermflusci.2023.110870 (2023).
26. Duan, F. & Wang, J.-J. Passive bionic motion of a flexible film in the wake of a circular cylinder: chaos and periodicity, flow–structure interactions and energy evolution. *J. Fluid Mech.* https://doi.org/10.1017/jfm.2024.327 (2024).
27. Wang, H., Zhao, C., Zeng, L., Mahbub Alam, M. & Tang, H. Control of the flow around a finite square cylinder with a flexible plate attached at the free end. *Phy. Fluids* https://doi.org/10.1063/5.0082181 (2022).
28. Yang, Y., Chen, Y., Li, Y., Chen, M. Z. Q. & Wei, Y. Bioinspired Robotic Fingers Based on Pneumatic Actuator and 3D Printing of Smart Material. *Soft Rob.* **4**(2), 147–162. https://doi.org/10.1089/soro.2016.0034 (2017).
29. Shintake, J., Schubert, B., Rosset, S., Shea, H. R., & Floreano, D. Variable stiffness actuator for soft robotics using dielectric elastomer and low-melting-point alloy.In *2015 IEEE/RSJ International Conference on Intelligent Robots and Systems (IROS)*, 1097-1102 (2015).
30. Okatani, Y., Nishida, T., & Tadakuma, K. Development of universal robot gripper using MRα fluid. In *2014 Joint 7th International Conference on Soft Computing and Intelligent Systems (SCIS) and 15th International Symposium on Advanced Intelligent Systems (ISIS)*, (2014).
31. Brown, E. et al. Universal robotic gripper based on the jamming of granular material. *Proc. Natl. Acad. Sci.* **107**, 18809–18814. https://doi.org/10.1073/pnas.1003250107 (2010).
32. Amend, J. R., Brown, E., Rodenberg, N., Jaeger, H. M. & Lipson, H. A positive pressure universal gripper based on the jamming of granular material. *IEEE Trans. Rob.* **28**(2), 341–350. https://doi.org/10.1109/TRO.2011.2171093 (2012).
33. Ranzani, T., Gerboni, G., Cianchetti, M. & Menciassi, A. A bioinspired soft manipulator for minimally invasive surgery. *Bioinspir. Biomim.* **10**(3), 035008. https://doi.org/10.1088/1748-3190/10/3/035008 (2015).

34. Cavallo, A., Brancadoro, M., Tognarelli, S. & Menciassi, A. A soft retraction system for surgery based on ferromagnetic materials and granular jamming. *Soft Rob.* **6**(2), 161–173. https://doi.org/10.1089/soro.2018.0014 (2018).
35. Fitzgerald, S. G., Delaney, G. W. & Howard, D. A review of jamming actuation in soft robotics. *Actuators* **9**(4), 104 (2020).
36. Kawamura, S., Yamamoto, T., Ishida, D., Ogata, T., Nakayama, Y., Tabata, O., & Sugiyama, S. Development of passive elements with variable mechanical impedance for wearable robots. In *Proceedings 2002 IEEE International Conference on Robotics and Automation (Cat. No.02CH37292)* (2002).
37. Bureau, M., Keller, T., Perry, J., Velik, R., & Veneman, J. F. Variable Stiffness Structure for limb attachment. In *2011 IEEE International Conference on Rehabilitation Robotics*, (2011).
38. Kim, Y. J., Cheng, S., Kim, S. & Iagnemma, K. A Novel layer jamming mechanism with tunable stiffness capability for minimally invasive surgery. *IEEE Trans. Rob.* **29**(4), 1031–1042. https://doi.org/10.1109/TRO.2013.2256313 (2013).
39. Choi, W. H., Kim, S., Lee, D. & Shin, D. Soft, multi-dof, variable stiffness mechanism using layer jamming for wearable robots. *IEEE Robot. Autom. Lett.* **4**(3), 2539–2546. https://doi.org/10.1109/LRA.2019.2908493 (2019).
40. Ibrahimi, M., Paternò, L., Ricotti, L. & Menciassi, A. A layer jamming actuator for tunable stiffness and shape-changing devices. *Soft Rob.* **8**(1), 85–96. https://doi.org/10.1089/soro.2019.0182 (2020).
41. Narang, Y. S., Vlassak, J. J. & Howe, R. D. Mechanically versatile soft machines through laminar jamming. *Adv. Func. Mater.* **28**(17), 1707136. https://doi.org/10.1002/adfm.201707136 (2018).
42. Narang, Y. S., Aktaş, B., Ornellas, S., Vlassak, J. J. & Howe, R. D. Lightweight highly tunable jamming-based composites. *Soft Rob.* **7**(6), 724–735. https://doi.org/10.1089/soro.2019.0053 (2020).
43. Aktaş, B., Narang, Y. S., Vasios, N., Bertoldi, K. & Howe, R. D. A Modeling framework for jamming structures. *Adv. Func. Mater.* **31**(16), 2007554. https://doi.org/10.1002/adfm.202007554 (2021).
44. Caruso, F., Mantriota, G., Moramarco, V. & Reina, G. Layer jamming: Modeling and experimental validation. *Int. J. Mech. Sci.* **251**, 108325. https://doi.org/10.1016/j.ijmecsci.2023.108325 (2023).
45. Caro, F. & Carmichael, M. G. A review of mechanisms to vary the stiffness of laminar jamming structures and their applications in robotics. *Actuators* **13**(2), 64 (2024).
46. Blanc, L., Pol, A., François, B., Delchambre, A., Lambert, P., & Gabrieli, F. Granular Jamming as Controllable Stiffness Mechanism for Medical Devices. In Giovine, P., Mariano, P. M., & Mortara, G. (Eds). *Micro to MACRO Mathematical Modelling in Soil Mechanics* (2018).
47. Vasios, N., Narang, Y., Aktaş, B., Howe, R. & Bertoldi, K. Numerical analysis of periodic laminar and fibrous media undergoing a jamming transition. *Eur. J. Mech. A. Solids* **75**, 322–329. https://doi.org/10.1016/j.euromechsol.2019.02.002 (2019).
48. Chen, Y., Ryu, J., Liu, Y. & Sung, H. J. Flapping dynamics of vertically clamped three-dimensional flexible flags in a Poiseuille flow. *Phy. Fluids.* https://doi.org/10.1063/5.0010835 (2020).

Acknowledgements

The authors wish to acknowledge the support given to them by the National Natural Science Foundation of China through Grant No. 52078505 and the Hunan Provincial Natural Science Foundation of China through Grant No. 2022JJ30736.

Author contributions

Y. designed the experimental methodology, assisted with the experimental setup and data collection, and performed preliminary data analysis. Y. validated the experimental results and revised the manuscript. G. designed the research, performed the experiments, and analyzed the data. G. developed the theoretical model, conducted the experiments on the Layer Jamming Plate (LJP) with tunable stiffness, and investigated its near wake structure in cross flow. G. also wrote the main manuscript text and prepared all the figures. W. (Advisor) provided guidance on the research design, interpretation of results, and manuscript preparation. W. contributed significantly to the discussion and revision of the manuscript. All authors discussed the results, contributed to the interpretation of the data, and reviewed and approved the final version of the manuscript.

Declarations

Competing interests

The authors declare no competing interests.

Additional information

Correspondence and requests for materials should be addressed to H.W.

Reprints and permissions information is available at www.nature.com/reprints.

Publisher's note Springer Nature remains neutral with regard to jurisdictional claims in published maps and institutional affiliations.